Heterogeneous Uptake of Sulfur Dioxide On Aluminum and Magnesium Oxide Particles

A. L. Goodman, P. Li, C. R. Usher, and V. H. Grassian*

Departments of Chemistry and Chemical and Biochemical Engineering, University of Iowa, Iowa City, Iowa 52246

Received: December 7, 2000; In Final Form: April 11, 2001

In this study, the heterogeneous uptake of SO_2 on α-Al_2O_3 and MgO particles at 296 K was investigated. Transmission FT-IR experiments reveal that under dry conditions SO_2 reacts with α-Al_2O_3 and MgO to form strongly adsorbed bisulfite, HSO_3^-(aq), and sulfite, SO_3^{2-}(aq), on α-Al_2O_3 and sulfite on MgO. To quantify the uptake of SO_2 under dry conditions, heterogeneous uptake coefficients were measured with a Knudsen cell reactor. The Knudsen cell data were modeled to account for gas diffusion in to the underlying layers and surface saturation. The initial uptake coefficient, γ_o, is calculated using the BET surface area of the powdered samples as diffusion of SO_2 into the powder is found to readily occur. Values of γ_o were determined to be $9.5 \pm 0.3 \times 10^{-5}$ and $2.6 \pm 0.2 \times 10^{-4}$ for SO_2 uptake on α-Al_2O_3 and MgO, respectively, at 296 K under dry conditions at a gas concentration near 1×10^{11} molecules/cm^3. Additionally, water uptake on sulfite-coated α-Al_2O_3 and sulfite-coated MgO particles was investigated with FT-IR spectroscopy. In the presence of adsorbed water, some of the adsorbed sulfite converted to sulfate on MgO but not on α-Al_2O_3. Atmospheric implications of these studies on SO_2 uptake on mineral dust aerosol are discussed.

Introduction

Gas-phase nitrogen and sulfur oxides can react with mineral aerosol to form particulate nitrate and sulfate. Recent atmospheric modeling studies have suggested that mineral aerosols have a significant impact on the chemistry of trace tropospheric gases, such as nitrogen and sulfur oxides.[1,2] Analysis of aerosol particles offers support of this suggestion as mineral aerosols are often found to be coated with sulfates and nitrates.[3−14] As a result, the mechanisms and reaction probability or uptake coefficient of trace tropospheric gases on mineral aerosols have been under investigation.[15−24]

Reaction of SO_2 on mineral aerosols is complicated because the mechanism for SO_2 oxidation on mineral particles to form sulfate is uncertain.[1] In the troposphere, gas-phase SO_2 reacts to produce sulfur trioxide, which is then rapidly converted to sulfuric acid in the presence of water vapor according to reactions 1 and 2.[25]

$$SO_2 + OH + O_2 \rightarrow SO_3 + HO_2 \quad (1)$$

$$SO_3 + H_2O \rightarrow H_2SO_4 \quad (2)$$

SO_3 in the marine boundary layer is oxidized to sulfate by O_3 and H_2O_2 on sea salt aerosol.[26−34] Aqueous-phase oxidation of SO_2 in liquid droplets and in clouds is also an important process.[35−42] Maahs reports that in aqueous aerosols sulfite and bisulfite may react as follows[43]

$$SO_3^{2-} + O_3 \rightarrow SO_4^{2-} + O_2 \quad (3)$$

and

$$HSO_3^- + H_2O_2 \rightarrow HSO_4^- + H_2O \quad (4)$$

Atmospheric sulfate particles are known to play a role in the global climate by scattering solar radiation and increasing the number of cloud condensation nuclei.[44,45] Sulfate-coated mineral dust particles can change this impact as they participate in the hygroscopic deliquescence and efflorescence cycles.[46,47]

In this study, the heterogeneous uptake of SO_2 on two types of oxide particles, α-Al_2O_3 and MgO, is investigated in order to gain some insight into the heterogeneous uptake of SO_2. α-Al_2O_3 and MgO are characterized as acidic and basic oxides, respectively, and are used here as models for mineral aerosol found in the troposphere. Transmission FT-IR spectroscopy and UV−vis diffuse reflectance spectroscopy were used to gain some mechanistic insight into SO_2 uptake. Knudsen cell experiments were done in order to quantify the rates of SO_2 uptake in terms of an initial heterogeneous uptake coefficient, γ_o.

Experimental Section

For FT-IR measurements, oxide samples were prepared by either pressing or spraying an oxide/water slurry onto half of a tungsten grid (Buckbee Mears, 100 lines/in. tungsten mesh wire widths of 0.0015″ and thickness of 0.002″). The other half of the grid was left blank for gas-phase measurements. The grid half coated with the oxide powder was placed inside the infrared cell. The infrared cell used in this study is modified from the design used in previous studies.[18,19] The modified infrared cell consists of a stainless steel cube (2.75″) with two germanium windows and a sample holder. The inside of the stainless steel cube is coated with Teflon in order to avoid gas decomposition on the walls of the infrared cell. The oxide samples prepared on the tungsten grid are secured inside the infrared cell by Teflon coated sample holder jaws. The infrared cell is connected to a vacuum chamber through a Teflon tube and a glass gas manifold with ports for gas introduction and two absolute pressure transducers (range 0.001 to 10.000 Torr and 0.1 to 1000.0 Torr). The total volume of the system is 1506 ± 3 mL (infrared cube

* To whom correspondence should be addressed.

10.1021/jp004423z CCC: $20.00
Published on Web 06/02/2001

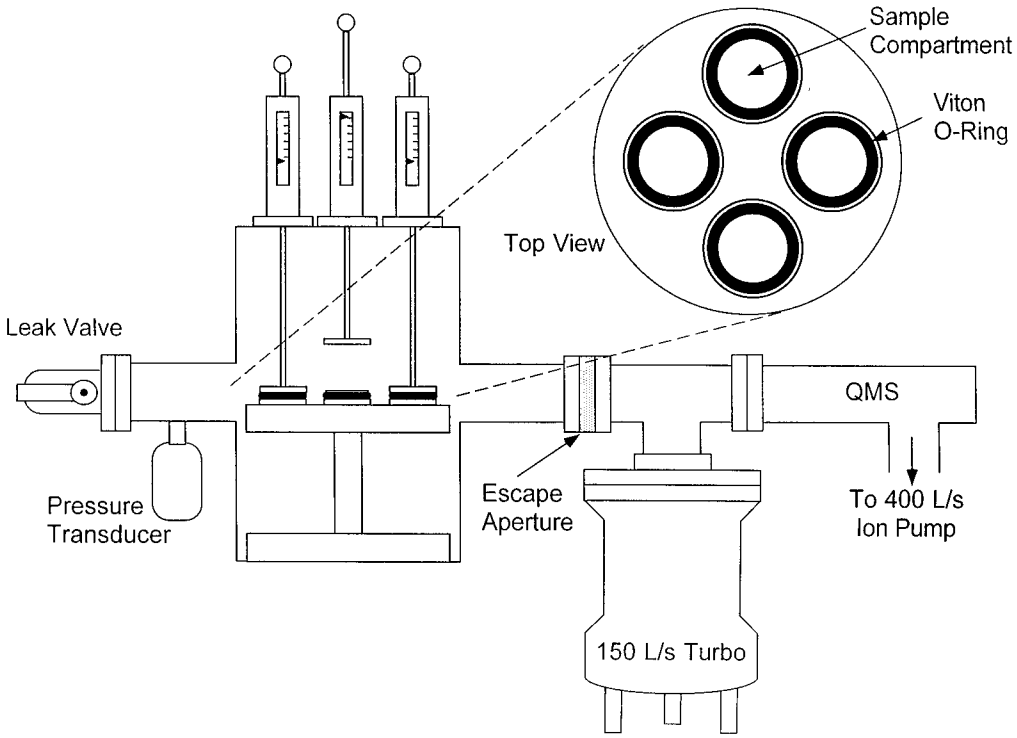

Figure 1. Multisample Knudsen cell apparatus used to measure heterogeneous uptake coefficients.

177 ± 2 mL and a glass gas-manifold 1329 ± 1 mL). The vacuum chamber consists of a two stage pumping system; a turbo-molecular/mechanical pump for pumping down to 10^{-7} Torr and a mechanical pump for rough pumping down to 10^{-3} Torr.

The infrared cell is mounted on a linear translator inside the FT-IR spectrometer. The translator allows both halves of the grid, the blank side for gas phase measurements and the oxide coated side for surface measurements, to be probed by simply moving the infrared cell through the IR beam path. Infrared spectra were recorded with a single beam Mattson RS-10000 spectrometer equipped with a narrow band MCT detector. Typically 250 scans were collected with an instrument resolution of 4 cm^{-1} in the spectral range extending from 750 to 4000 cm^{-1}.

Heterogeneous uptake coefficients were measured with a Knudsen cell reactor. A Knudsen cell reactor consists of a chamber with an isolated sample compartment and a small orifice through which gas-phase reactant and product species can escape to be detected, usually by mass spectrometry. In a typical Knudsen cell experiment, the sample compartment is covered while the walls of the reactor are passivated and a steady state flow is established. Usually the pressure in the cell is kept low enough such that the mean free path of the molecules within the cell is greater than the cell dimensions so that boundary layer effects and homogeneous gas-phase collisions are minimized and can be neglected. The cell can be used at higher pressures, but to ensure molecular flow the mean free path must be at least a factor of 10 greater than the diameter of the escape aperture.[48] In the experiments described herein, an effective escape aperture of 0.0129 cm^2, which accounts for the Clausing factor, was used.[49] The escape constant, k_{esc}, for this aperture was determined to be 0.080 s^{-1} for SO_2.

For the experiments described herein, a Knudsen cell reactor coupled to a UTI, DetecTorr II quadrupole mass spectrometer was used to determine uptake coefficients on powdered samples. Although the Knudsen cell used has been described previously,[50] it has recently been modified to allow for the analysis of multiple samples (Figure 1). A stainless steel reducing cross (6−2.75″) now has four individual sample holders attached to a platform which rests on the bottom (6″) flange. All exposed interior surfaces are coated with Teflon to provide a chemically inert surface. Four Teflon coated aluminum disks attached to four linear translators serve as covers for each of the powdered samples. The geometric area of each of the four sample holders is 5.07 cm^2. Since the volume of the sample holder is much smaller than the total volume of 1750 cm^3 (<1%), no corrections are needed to account for volume change upon opening the sample compartment. The seal between the sample holders and the cover is made with viton O-rings. With this setup four samples of differing mass can now be analyzed in a single run.

To begin each experiment, sulfur dioxide was flowed for at least 10 min to passivate the system. The gas was introduced through a leak valve to a desired pressure, measured by an absolute pressure transducer (MKS 690 A.1 TRC with a range of 10^{-6} to 0.1 Torr). At this time the sample holder lids were in the closed position in order to prevent the oxide particles from being exposed SO_2. The SO_2 parent ion ($m/e = 64$) was monitored during these experiments. Other mass channels were monitored in addition to the parent ion, including H_2O ($m/e = 18$), CO_2 ($m/e = 44$), SO ($m/e = 48$), SO_3 ($m/e = 80$), and H_2SO_4 ($m/e = 98$).

It is very important that the powdered sample be evenly applied, covering the entire geometric area of the sample holder; otherwise the measured initial uptake coefficient may reflect the amount of uncovered/unreactive surface in the sample holder as well as the sample mass. For preparing thin samples of the powdered samples, both of these concerns were addressed by using an atomizer to spray an aqueous slurry of the sample onto a heated sample holder. As determined with an optical microscope, this spraying procedure ensured very even coverage of the powdered sample across the bottom of the sample holder. All experiments reported here were done at $T = 296$ K.

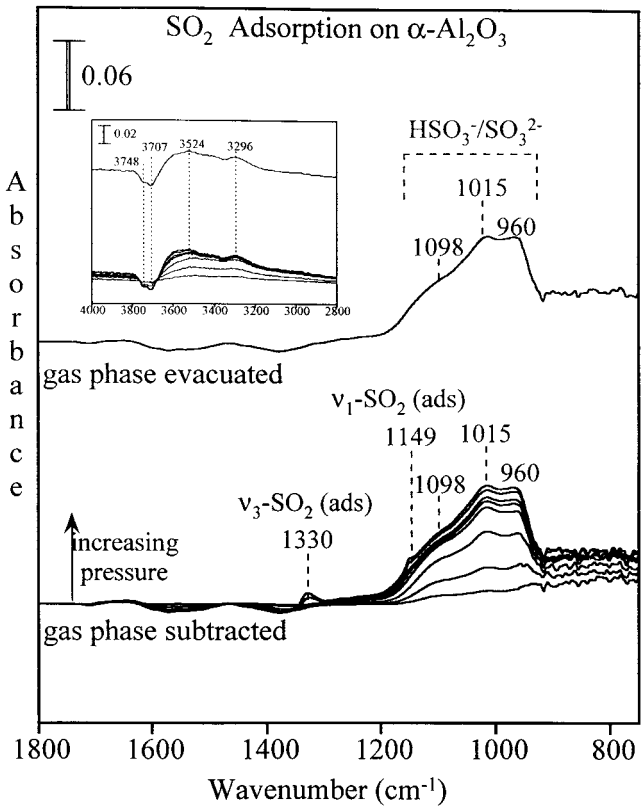

Figure 2. FT-IR spectra of α-Al_2O_3 upon exposure to SO_2 at various pressures. Spectra labeled "gas phase subtracted" were recorded in the presence of the gas phase at equilibrium pressures of 3, 4, 5, 8, 14, 44, 173, and 353 mTorr. The spectrum labeled "gas phase evacuated" was collected after evacuation of SO_2 at the highest pressure. The hydroxyl group region is shown in the inset.

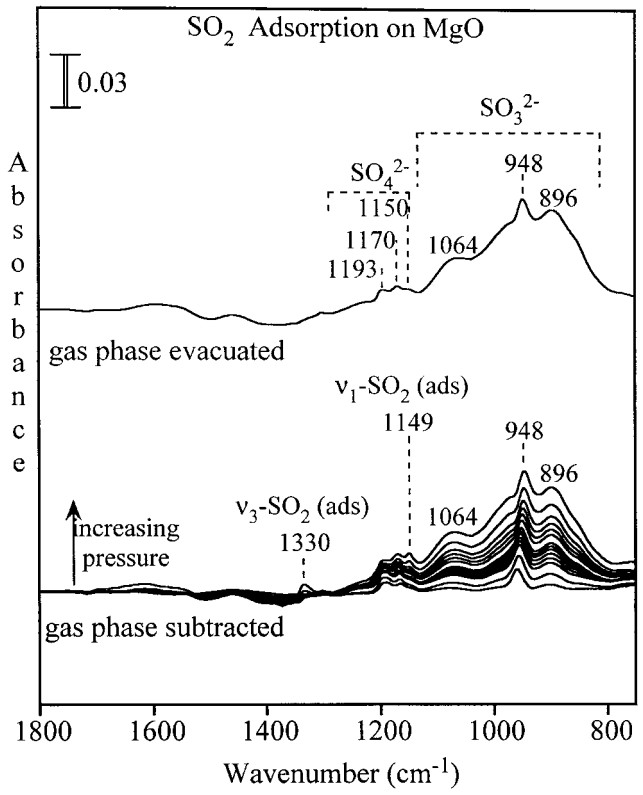

Figure 3. FT-IR spectra of MgO upon exposure to SO_2 at various pressures. Spectra labeled "gas phase subtracted" were recorded in the presence of the gas phase at equilibrium pressures of 3, 5, 7, 9, 11, 16, 23, 43, 89, 178, 353, 880, 2637, and 5275 mTorr. The spectrum labeled "gas phase evacuated" was collected after evacuation of SO_2 at the highest pressure.

The oxide powders used in this study were purchased from Alfa Aesar. The average particle diameters were determined from transmission electron micrographs to be 0.5 and 0.2 μm for α-Al_2O_3 and MgO, respectively. The surface areas of the particles were measured using a multipoint BET apparatus (Quantachrome 1200) and determined to be 14 and 15 m^2/g for α-Al_2O_3 and MgO, respectively. Distilled H_2O (Milli-Q) was degassed prior to use. Gaseous SO_2 (Matheson, 99.98 wt % min purity) was used as received.

Results

FT-IR Study of SO_2 Adsorption on α-Al_2O_3 and MgO Particles at 296 K. The FT-IR spectra following the reaction of SO_2 on α-Al_2O_3 and MgO particles at 296 K as a function of pressure between 3 and 353 mTorr are shown in Figures 2 and 3, respectively. In these experiments, α-Al_2O_3 and MgO particles were loaded in the glass-Teflon infrared system and evacuated to 10^{-7} Torr overnight. A known pressure of SO_2 was admitted in the infrared cell containing either α-Al_2O_3 or MgO particles. When the pressure of the gas reached equilibrium, two spectra were recorded, one of the gas phase and the other of the surface in the presence of the gas phase. Absorbance spectra of SO_2 adsorbed on α-Al_2O_3 and MgO particles were obtained by referencing an oxide sample spectrum after SO_2 was introduced into the infrared cell to an oxide background spectrum prior to adsorption. Gas-phase absorption bands measured through the blank grid could then be subtracted from the gas phase/adsorbate spectrum in order to obtain a spectrum of adsorbed SO_2 only.

Changes in the infrared spectra of the α-Al_2O_3 surface as a function of increasing SO_2 are clearly seen in Figure 2. Upon adsorption of SO_2 on α-Al_2O_3 particles, a broad absorption band between 900 and 1200 cm^{-1}, with features at 960, 1015 and 1098 cm^{-1}, is observed in the spectrum (Figure 2, gas-phase subtracted). This broad band grew in intensity as the SO_2 pressure was increased. When the α-Al_2O_3 particles were exposed to the highest SO_2 pressures investigated, 172 and 353 mTorr, two small bands at 1149 and 1330 cm^{-1} became apparent in the spectrum. Upon evacuation of gas-phase SO_2, the strong broad absorption band between 900 and 1200 cm^{-1} remained in the spectrum and the two weaker bands at 1149 and 1330 cm^{-1} disappeared. This indicates that the surface adsorbed species with the broad absorbance between 900 and 1200 cm^{-1} is chemisorbed on the α-Al_2O_3 particles and cannot be removed upon evacuation of the gas phase, while the weaker bands at 1149 and 1330 cm^{-1} are only present in the presence of the gas phase and are associated with a physisorbed species.

The inset of Figure 2 shows changes in the hydroxyl region upon adsorption of SO_2. There is the growth of a broad band with maxima at 3524 and 3296 cm^{-1} in the spectra which is still present upon evacuation of the gas phase. Negative features at 3748 and 3707 cm^{-1} indicate either loss of hydroxyl groups from the surface or that the hydroxyl groups are involved in hydrogen bonding.

The assignment of the vibrational bands of adsorbed sulfur dioxide has been discussed previously.[51−55] The broad absorption band between 900 and 1200 cm^{-1} in the α-Al_2O_3 spectrum is composed of more than one band and is assigned to the absorptions of sulfite and bisulfite on the surface. The two small adsorption bands at 1149 and 1330 cm^{-1} that disappear upon evacuation of the gas phase are assigned to the symmetric (ν_1) and asymmetric (ν_3) stretch, respectively, of weakly adsorbed

SO_2. These bands associated with weakly adsorbed SO_2 are shifted only slightly from their corresponding gas-phase values of 1151 and 1362 cm^{-1}.[56]

The infrared spectra obtained in this study following adsorption of SO_2 on α-Al_2O_3 agree well with other infrared studies reported in the literature. Mitchel et al.,[57] Karge and Dalla Lana,[58] and Chang[59] investigated SO_2 adsorption on γ-Al_2O_3 particles with infrared spectroscopy and found that SO_2 both weakly and strongly adsorbs onto γ-Al_2O_3. Two bands at 1330 and 1150 cm^{-1} were assigned to weakly adsorbed SO_2 and a broad band centered at 1060 cm^{-1} was assigned to strongly adsorbed SO_2 identified as a sulfite species. For highly hydroxylated alumina surfaces, such as the ones used here, bisulfite was identified on the surface as well. Possible surface reactions with SO_2 and surface hydroxyls and lattice oxygen atoms to form sulfite and bisulfite are presented in the Discussion.

Changes in the infrared spectra of the MgOsurface as a function of increasing SO_2 pressure are clearly seen in the spectra shown in Figure 3. The adsorption of SO_2 on MgO is similar to the adsorption of SO_2 on α-Al_2O_3 particles in that a strongly adsorbed species and weakly adsorbed SO_2 formed on MgO following exposure to gaseous SO_2. The strongly adsorbed species shows a strong broad absorption band between 800 and 1125 cm^{-1} with three features at 896, 948, and 1064 cm^{-1}. Weakly adsorbed SO_2, which was represented by absorption bands at 1149 and 1330 cm^{-1}, is only observed at highest pressures. In addition, three weak absorptions near 1193, 1170, and 1150 cm^{-1} also grew in intensity with increasing SO_2 pressure. This group of bands remained in the spectrum upon evacuation of SO_2 vapor. As discussed below, this group of absorption bands is assigned to the ν_3-stretching mode of bidentate surface-coordinated sulfate.

The broad band between 800 and 1125 cm^{-1} can be assigned to surface-coordinated sulfite following adsorption of SO_2 on MgO particles. This interpretation is in agreement with other studies for SO_2 adsorption on the basic oxides MgO and CaO. Using FT-IR photoacoustic spectroscopy, Martin et al. studied reaction of SO_2 on CaO particles.[60] Upon reaction of SO_2 on CaO at 25 °C, they observed a broad absorption band centered at 950 cm^{-1}. They assigned this band to the ν_3 and ν_1 stretching modes of surface sulfite. Babaeva et al. also studied adsorption of SO_2 on MgO particles.[61] They observed absorption bands at 1150 and 1335 cm^{-1} corresponding weakly adsorbed SO_2 following adsorption of SO_2 on MgO at 170 K. At room temperature, adsorption of SO_2 on MgO resulted in the formation of surface sulfite with absorption bands at 960 and 1050 cm^{-1}. At room temperature, weakly adsorbed SO_2 on MgO particles was barely detectable. Schoonheydt and Lunsford also report surface sulfite absorption bands at 975 and 1040 cm^{-1} following reaction of SO_2 on MgO at room temperature.[62] Gebel et al.[63] studied uptake of SO_2 on synthetic sea salt and found weakly adsorbed SO_2 near 1360 cm^{-1} and surface adsorbed sulfite near 960 cm^{-1} corresponding to the reaction of SO_2 on the $CaCO_3$ component of synthetic sea salt to give $CaSO_3$. In addition, the assignment of bidentate surface-coordinated sulfate on MgO particles is taken from that of Martin et al., who assigned three bands at 1157, 1130, and 1080 cm^{-1} that appeared following adsorption of SO_2 on CaO at 200 °C to the ν_3 stretching mode of bidentate SO_4^{2-}.[60]

Diffuse reflectance UV−vis spectroscopy provided further evidence that SO_2 reacts with α-Al_2O_3 and MgO particles to produce surface-coordinate sulfite. In the UV region, sulfite and bisulfite ion absorbs near 250 nm whereas sulfate does not.[64] UV−vis reflectance spectra following reaction of SO_2 on

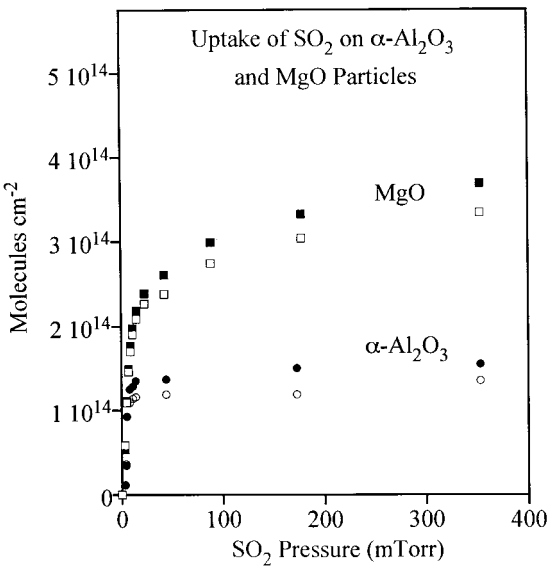

Figure 4. Total uptake of SO_2 on α-Al_2O_3 and MgO was determined as a function of SO_2 exposure.

α-Al_2O_3 and MgO particles shows features at 259 nm for α-Al_2O_3 and 252 nm for MgO indicate that surface-coordinated sulfite and/or bisulfite is present on the oxide surface.[65]

Total Uptake of SO_2 on α-Al_2O_3 and MgO Particles Determined by FT-IR and Volumetric Measurements. The infrared data for SO_2 adsorption on α-Al_2O_3 and MgO particles were further analyzed to determine the total uptake of SO_2 on these oxide particles at 296 K. Adsorption isotherms curves are shown in Figure 4, where the coverage of adsorbed SO_2 on α-Al_2O_3 and MgO particles (molecules cm^{-2}) is plotted against the equilibrium pressure of SO_2 (mTorr) (Figure 4, α-Al_2O_3 solid circles, MgO solid squares). The absorption bands of adsorbed SO_2 on α-Al_2O_3 and MgO particles between 1250 and 785 cm^{-1} were integrated as a function of SO_2 pressure. The integrated absorbance was then calibrated to coverages in molecules per squared centimeter through volumetric measurements, i.e., by measuring the pressure difference between SO_2 expanded into an empty infrared cell versus expanded into the infrared cell containing the adsorbent, (α-Al_2O_3 or MgO). The expansion of SO_2 into the infrared cell with no oxide sample present was also done as a function of increasing SO_2 pressure. The pressure difference between gaseous SO_2 admitted into the infrared cell with and without the oxide was determined. Through the ideal gas law, the pressure difference can be related to the number of molecules of SO_2 adsorbed on the oxide particles. The total number of molecules adsorbed was then divided by the total surface area of the adsorbent to give SO_2 coverages in units of molecules cm^{-2}. A plot comparing the uptake of SO_2 in terms of molecules cm^{-2}, which was calculated by volumetric measurements, and of integrated absorbance, which was determined from integrating absorption bands of adsorbed SO_2, versus SO_2 equilibrium pressure followed the same curve. Therefore, the integrated absorbance is calibrated to molecules cm^{-2} and plotted against SO_2 equilibrium pressure.

Upon exposure of α-Al_2O_3 to SO_2, the uptake is seen to increase rapidly and then saturates at a coverage of 1.5×10^{14} molecules cm^{-2}. SO_2 adsorption on MgO increases rapidly to 2.5×10^{14} molecules cm^{-2} at a pressure of 25 mTorr. As higher SO_2 pressures are reached the uptake levels off at a coverage of 4.0×10^{14} molecules cm^{-2} near 350 mTorr but does not appear to completely saturate. The coverage of adsorbed SO_2 immediately after evacuation of gas-phase SO_2 was also determined (Figure 4, α-Al_2O_3 open circles, MgO open

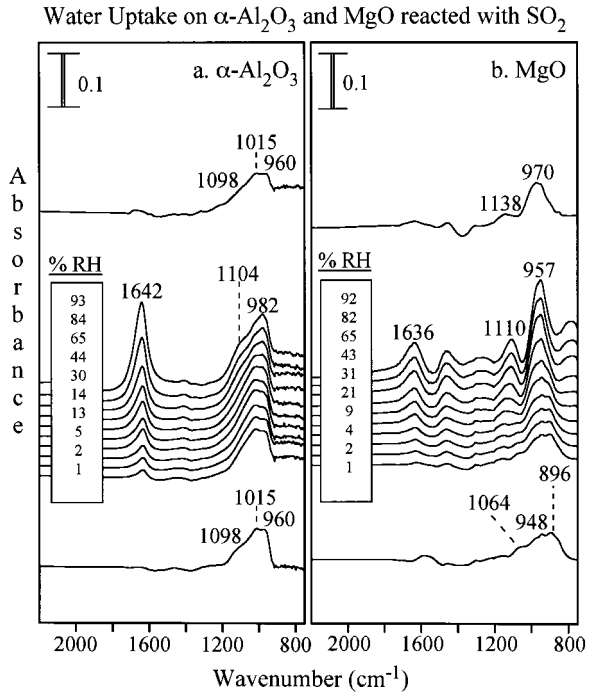

Figure 5. FT-IR spectra of water adsorption on SO_2 reacted (a) α-Al_2O (left panel) and (b) MgO (right panel) as a function of relative humidity.

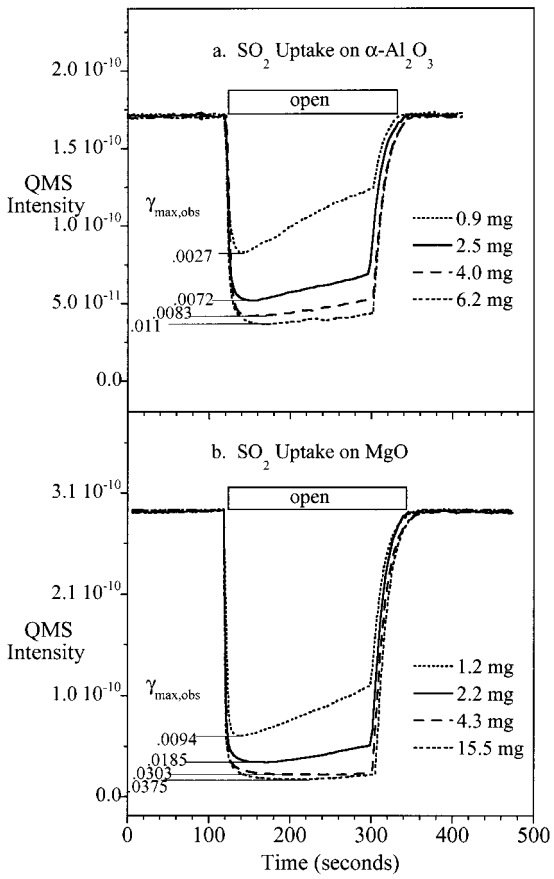

Figure 6. Knudsen cell data showing the heterogeneous uptake of SO_2 on (a) α-Al_2O and (b) MgO as a function of sample mass. The maximum observed uptake, calculated using eq 6, is shown to be a function of sample mass.

squares). The integrated absorbance decreases after gas-phase SO_2 is evacuated from the infrared cell by approximately 10% at the highest coverages. Thus, the adsorption of SO_2 on these two oxides is approximately 90% irreversible and there is a hysteresis observed in the adsorption isotherm.

Our calculations for the coverage of SO_2 on oxide particles is comparable to the work of Stark et al. who investigated the uptake of SO_2 on MgO pellets between 0 and 800 Torr of SO_2.[66] Using a cross-sectional area of 1.92 nm^2 for SO_2, they calculated a monolayer coverage of 5.2×10^{14} molecules cm^{-2} on MgO pellets. They found that upon evacuation of gas-phase SO_2, the coverage of SO_2 dropped to 5.0×10^{14} molecules cm^{-2}. Thus, they determined that 4% of the total amount of SO_2 was weakly adsorbed.

Role of Water in the Reaction of SO_2 on α-Al_2O_3 and MgO Particles. Since it is becoming increasingly clear through laboratory studies that surface adsorbed water plays a role in the heterogeneous chemistry of trace atmospheric gases such as nitric acid,[67−71] the adsorption of water on sulfite coated α-Al_2O_3 and MgO was investigated. In these experiments, α-Al_2O_3 and MgO particles were reacted with SO_2 until the surface was saturated with surface-coordinated sulfite. Gas-phase SO_2 was then evacuated from the infrared cell. Water was then added to the infrared cell containing α-Al_2O_3 and MgO particles as a function of increasing relative humidity between 1 and 93% RH. At the highest relative humidity (93% RH), water vapor was evacuated and a spectrum was recorded. As can be seen in the spectra shown in Figure 5, as the water vapor pressure increased, an absorption band near 1640 cm^{-1}, corresponding to the bending mode of surface adsorbed water, grows in. This band has been used to determine the coverage of adsorbed water layers.[71] Except for the growth of the band associated with the water bending mode, only small changes in the α-Al_2O_3 spectra are seen as a function of RH. There is a slight shift in the band at 1098−1104 cm^{-1} as higher relative humidity and some small changes in the shape of the broad absorpiton band that extends from 900 to 1150 cm^{-1}. The absorption bands at 1015 and 960 cm^{-1}, assigned to surface-coordinated sulfite, combined into one band at 982 cm^{-1} as water vapor pressure increased. These frequency shifts may be due to water-solvation effects as was observed for nitrated α-Al_2O_3 particle surfaces.[71,72] Upon evacuation of gas-phase water (top spectrum), the spectrum reverts back to the original surface-coordinated sulfite spectrum with absorption bands at 1098, 1015, and 960 cm^{-1}. This result is in agreement with those of Karge and Dalla Lana[58] in that strongly adsorbed SO_2 was not affected much by H_2O adsorption.

As water vapor was added to the infrared cell containing MgO particles that had been previously reacted with SO_2, the bending mode vibration of surface adsorbed water becomes apparent as it did on the α-Al_2O_3 surface. In addition, new bands at 1110 and 957 cm^{-1} appear in the spectrum. These new absorption bands are assigned to water-solvated sulfite and sulfate on the surface.[73,74] Upon evacuation, absorption bands at 1138 and 970 cm^{-1} remain in the spectrum. Most likely there is a mixture of surface-coordinated sulfite and sulfate that remains on the MgO surface upon evacuation of water vapor. Thus upon addition of water, some surface-coordinated sulfite is converted to surface-coordinated sulfate on the MgO surface. It is estimated that ∼5−10% of the sulfite is converted to sulfate. The absorption band near 1460 cm^{-1} has been discussed elsewhere and is due to water solvated carbonate on the MgO surface.[71]

Knudsen Cell Study of SO_2 Adsorption on α-Al_2O_3 and MgO Particles at 296 K. Knudsen cell experiments were conducted in order to quantify the uptake of SO_2 on these two oxide surfaces at 296 K. The Knudsen cell data for the uptake of sulfur dioxide on α-Al_2O_3 and MgO are shown in Figure 6. The data are presented in terms of QMS intensity of the parent

TABLE 1: Uptake Coefficients Determined for Heterogeneous Reaction of SO_2 on α-Al_2O_3 and MgO Particles

oxide	sample mass (mg)	$\gamma_{max,obs}$[a]	$\gamma_{max,BET}$[b]	$\gamma_{o,model}$[c]
α-Al_2O_3	0.9	2.7×10^{-3}	1.1×10^{-4}	1.0×10^{-4}
	2.5	7.2×10^{-3}	1.3×10^{-4}	
	4.0	8.3×10^{-3}	7.5×10^{-5}	
	6.2	1.1×10^{-2}	6.4×10^{-5}	
MgO	1.2	9.4×10^{-3}	2.7×10^{-4}	2.7×10^{-4}
	2.2	1.9×10^{-2}	2.8×10^{-4}	
	4.3	3.0×10^{-2}	2.4×10^{-4}	
	15.5	3.8×10^{-2}	8.2×10^{-5} [d]	

[a] The observed uptake coefficient is calculated using eq 6. [b] The BET uptake coefficient is calculated as follows $\gamma_{max,BET} = \gamma_{max,obs}(A_s/A_{BET})$, where A_{BET} = mass × S_{BET}. S_{BET} is equal to 140 cm^2/mg and 150 cm^2/mg for α-Al_2O_3 and MgO, respectively. [c] The initial uptake coefficient determined from the computer simulation using the layer by layer model. [d] Masses outside the linear mass regime. See text for further detail. Average of $\gamma_{max,BET}$ for masses in the linear regime; $(9.5 \pm 0.3) \times 10^{-5}$ and $(2.6 \pm 0.2) \times 10^{-4}$ for α-Al_2O_3 and MgO, respectively.

ion, *m*/*e* 64, for SO_2 versus time. Four different samples are shown for each of the oxide samples, each of a different mass. The data for each sample have been overlayed during the time the oxide samples are exposed to SO_2 as indicated by a rectangle labeled "open". The experiments show that after an initial steady-state flow of SO_2 is achieved there is a large drop in the ion signal for the parent ion when the oxide particles are exposed to SO_2. The data also show that the extent of the drop in the signal depends on the mass of the oxide sample.

Using the steady-state derived Knudsen cell equation for determining the heterogeneous uptake coefficient for gases on a solid surface, the observed uptake coefficient can be calculated as follows[48,75]

$$\gamma_{obs} = \frac{A_h}{A_s}\frac{(I_o - I)}{I} \tag{5}$$

where A_h is the effective area of the escape aperture or escape hole, A_s the geometric area of the sample holder, and I_o and I are the QMS intensity measured with the sample covered and sample exposed, respectively. The uptake coefficient as calculated by eq 5 is referred to as γ_{obs}, the observed uptake coefficient.

The maximum observed heterogeneous uptake coefficient was determined for each sample and the value is shown in Figure 6. The maximum value of the uptake coefficient, often reported as the initial uptake coefficient, is taken as the point where the SO_2 parent ion signal intensity is a minimum. The maximum value, $\gamma_{max,obs}$, was calculated for each mass using eq 5 above and is given for each mass in both Figure 6 and Table 1. It is seen that the maximum value depends on sample mass, and therefore upon sample thickness and that the maximum value occurs at longer times as the sample mass increases. For the thinner samples, γ_{obs} reaches a maximum and then the value decreases as the sample is continuously exposed to gaseous SO_2.

In the derviation of eq 5, it is assumed that the total number gas/surface collisions is taken as the flux of molecules to the geometric area of the sample holder; each time a molecule comes near the sample, it hits only once and only with the very top layer of the sample, which could be expected if the sample were a liquid or a single crystal. However, this is not the case for the samples used in these experiments, which are powders and thus inherently porous in nature. This assumption that gas molecules interact only once and only with the top layer is an oversimplification that does not adequately describe the data collected in these experiments as discussed below.

It has been previously shown that the observed mass dependence involves the diffusion of the reactant gas to underlying layers, resulting in an increase in the number of collisions with the interior surfaces of the particles in the sample.[50] The increased surface area, and thus the increased number of collisions, must be accounted for when determining the uptake coefficient. It is clear from the data presented that several kinetic steps are occurring simultaneously: adsorption, diffusion, and surface saturation, which is most easily seen for the smallest masses. To understand the observed mass dependence, the shift in the maximum of the observed uptake coefficient and the decrease in γ_{obs} with time due to surface saturation for thinner samples but not thicker samples, we have simulated the time dependent uptake in order to extract an initial uptake coefficient from the data.

The effects of surface coverage and saturation on the measured uptake coefficient have not been previously considered for Knudsen cell experiments. Here we will consider the effects of surface coverage and saturation in determining an initial uptake coefficient, γ_o, using a simple site-blocking, Langmuir-type adsorption mechanism. In this case, the uptake coefficient is a function of coverage and takes the form

$$\gamma = \gamma_o(1 - \theta) \tag{6}$$

where γ is the uptake coefficient, θ is the surface coverage, and γ_o is the uptake coefficient in the limit of zero surface coverage. Assuming a first-order rate process in the gas pressure and the number of available surface sites $(1 - \theta)$, the rate of adsorption can be written as

$$\frac{dN_a}{dt} = k_a p N_s(1 - \theta) \tag{7}$$

where N_a, is the number of adsorbed molecules, k_a is the rate constant for adsorption, p is the pressure of the gas, N_s is the total number of surface sites that can be populated at that pressure and θ is the fractional coverage. If the pressure of the gas is taken to be nearly constant in this flow experiment (i.e., under conditions such that the change in the pressure is small), then the rate of the reaction can be analyzed in terms of a pseudo-first-order process with respect to surface sites. With this assumption, and since $N_a = N_s\theta$ and $dN_a = N_s\, d\theta$, eq 7 can be solved and the solution of the differential expression is

$$\gamma = \gamma_o\, e^{-at} \tag{8}$$

where $a = k_a p$.

The rate of adsorption can also be written as

$$\frac{dN_a}{dt} = \gamma Z = \gamma\frac{p}{\sqrt{(2\pi mkT)}} = \gamma_o(1 - \theta)\frac{p}{\sqrt{(2\pi mkT)}} \tag{9}$$

where Z is the rate of collisions of the gas molecules with the unit surface area, m is the molecular mass of the gas molecule, k is the Boltzmann constant, T is the absolute temperature. By comparing eq 7 to eq 9, the rate constant becomes

$$k_a = \frac{\gamma_o}{N_s\sqrt{(2\pi mkT)}} \tag{10}$$

Therefore,

$$a = k_a p = \frac{\gamma_o p}{N_s\sqrt{(2\pi mkT)}} = 3.154 \times 10^{19}\frac{\gamma_o p}{N_s\sqrt{(MT)}} \quad (11)$$

where p is in units of mTorr, N_s is in units of molecules cm^{-2}, M is the molar mass of the gas in units of gram per mole, and T is the absolute temperature in Kelvin.

The time dependent uptake coefficient given in eq 8 with the value of a given in eq 11 can now be put into the rate equations derived for heterogeneous uptake measured with the Knudsen cell technique. The rate of gas flow in a Knudsen cell reactor following time-independent uptake, i.e., γ is constant, can be written as[76]

$$\frac{dN}{dt} = \text{Flow}_{in} - \text{Flow}_{out} - \text{Flow}_{uptake} = k_{esc}N_o - k_{esc}N - \gamma\frac{A_s}{A_h}k_{esc}N \quad (12)$$

Substituting eq 8 into eq 12 we get

$$\frac{dN}{dt} = k_{esc}N_o - k_{esc}N - k_{esc}N\frac{A_s}{A_h}(\gamma_o e^{-at}) \quad (13)$$

If a mass spectrometer is used to monitor gas flow, this expression can be written in terms of a normalized mass spectral intensity as

$$\frac{dI}{dt} = k_{esc} - k_{esc}I - k_{esc}I\frac{A_s}{A_h}(\gamma_o e^{-at}) \quad (14)$$

For heterogeneous uptake on powdered samples, the uptake coefficient is time-dependent for two reasons. First, as described above, surface saturation is time dependent. Second, as described below, gas diffusion into the underlying layers of the sample will also contribute.

A powdered sample consists of many layers of particles. We have developed a layer-by-layer approach to describe the uptake of gas by a porous solid.[76] The uptake on each of the individual layers can be described by eq 8, but the gas molecules do not reach all the individual layers at the same time due to the diffusion time through the powder. The first layer is unique because there is no diffusion time in the powder. The uptake can be described for each layer, n, as follows

$$\text{First Layer:} \quad \gamma_1 = \gamma_0 e^{-at}$$

$$\text{Second Layer:} \quad \gamma_2 = \begin{cases}\gamma_0 e^{-a(t-t_2)}, & \text{if } t \geq t_2\\ 0, & \text{if } t < t_2\end{cases}$$

$$\text{Third Layer:} \quad \gamma_3 = \begin{cases}\gamma_0 e^{-a(t-t_3)}, & \text{if } t \geq t_3\\ 0, & \text{if } t < t_3\end{cases}$$

$$n\text{th Layer:} \quad \gamma_n = \begin{cases}\gamma_0 e^{-a(t-t_n)}, & \text{if } t \geq t_n\\ 0, & \text{if } t < t_n\end{cases} \quad (15)$$

where t_2 is the time it takes for gas molecules to diffuse to the second layer, t_3 is the time to get to the third layer, etc. If at any time $t < t_n$, i.e., before the gas molecules can reach the nth layer, there is no uptake on that layer so the uptake coefficient is set equal to zero. After the gas molecules reach the layer, the uptake process follows eq 8.

The time it takes to get to each layer can be determined from the diffusion time through the powder. The root-mean-square distance l traveled by molecules with effective diffusion constant through the powder D_{eff} in time t is given by[77]

$$l = \sqrt{2D_{eff}t} \quad (16)$$

Therefore, the time it takes to diffuse is

$$t = \frac{l^2}{2D_{eff}} \quad (17)$$

For a powder sample with mass m_s and bulk density ρ packed in a sample holder with geometric area, A_s, the total thickness, L, is given by

$$L = \frac{m_s}{\rho A_s} \quad (18)$$

If the specific BET area of the powder sample is S_{BET}, the total BET area of the powder sample is $m_s S_{BET} = A_{BET}$, the whole powder sample can then be treated as j layers of A_s surfaces stacked one on top of the other with

$$j = \frac{A_{BET}}{A_s} \quad (19)$$

and the distance between two adjacent A_s surfaces is

$$d = \frac{L}{j} = \frac{1}{S_{BET}\rho} \quad (20)$$

It should be noted that it does not matter how the layers are defined as long as the total surface area, A_{BET}, is kept constant.

The Knudsen cell equation in terms of the normalized mass spectral intensity then becomes

$$\frac{dI}{dt} = k_{esc} - k_{esc}I - k_{esc}I\frac{A_s}{A_h}\left\{\sum_{i=0}^{j}\gamma_o, \text{ if}\left[t < \frac{\left(\frac{i}{j}L\right)^2}{2D}, *0, \text{ or } *e^{-a[t-((i/j)L)^2/2D_{eff}]}\right]\right\} \quad (21)$$

where

$$i = n - 1 \quad (22)$$

and

$$t_i = \frac{\left(\frac{i}{j}L\right)^2}{2D_{eff}} \quad (23)$$

The *if* clause in eq 21 can be easily implemented in many mathematical packages available today (such as MATHCAD). Equation 21 can be used to model the experimental observations such as the mass and time dependence of the observed uptake. In this equation, the initial uptake coefficient, γ_o, and the effective diffusion constant, D_{eff}, are fitting parameters. Most other parameters in the equation are experimental parameters (pressure, k_{esc}, mass, ρ, A_s, A_{BET}, and mass). The maximum coverage (N_s) at that pressure can be determined from the experimental data (vide infra). As will be shown, there is a decrease in the gas pressure in the Knudsen cell when molecules adsorb on the powder. To take this decrease in pressure into account the a term can be modified to include the pressure change, where I is the mass spectral intensity at any time t and

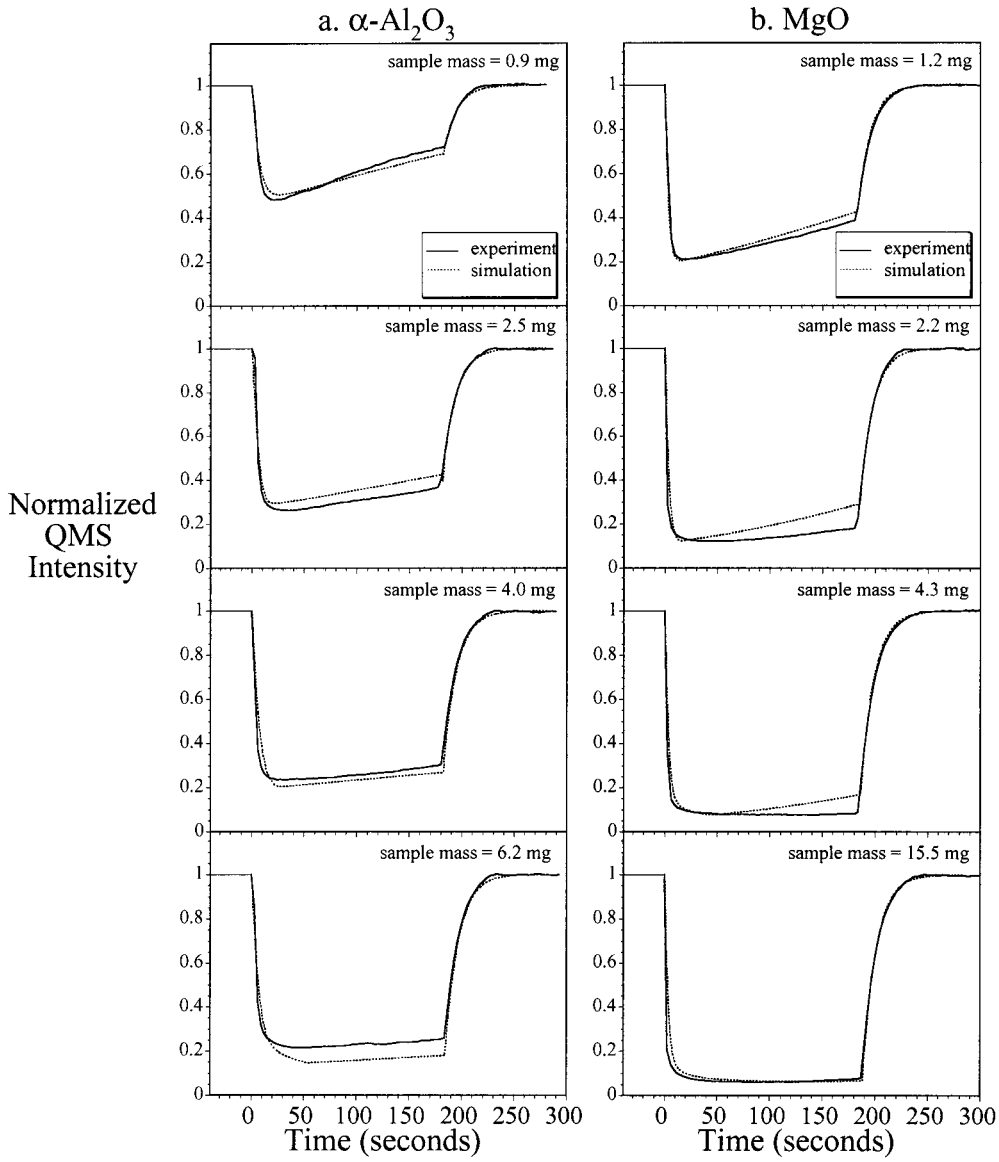

Figure 7. A comparison of the experimental Knudsen cell data and computer simulated data using the layer-by-layer uptake model, is shown for SO_2 uptake on (a) α-Al_2O_3 and (b) MgO. The experimental and fitting parameters used in the model are given in Table 2.

I_o is the initial mass spectral intensity before adsorption on the oxide surface. Thus, a now takes the form

$$a = \frac{\gamma_o p(I/I_o)}{N_s\sqrt{(2\pi mkT)}}\,e = 3.154 \times 10^{19}\,\frac{\gamma_o p(I/I_o)}{N_s\sqrt{MT}} \qquad (24)$$

Before comparing the model and the experimental data, it is instructive to look at two limiting cases. The first case is when diffusion is slow and the uptake coefficient is large. In this case, as D_{eff} approaches zero then t_i, the time it takes to diffuse to underlying layers, goes to infinity. Thus, the exponential term goes to zero for all layers except for the top layer and uptake occurs on the top layer only. The second limiting case is for fast diffusion, as expected when the uptake coefficient is small. In this case, as D_{eff} becomes very large then the second term in the exponential goes to zero. The entire bracketed part of eq 21 then reduces to $jA_s\gamma_o\, e^{-at} = A_{BET}\,\gamma_o\, e^{-at}$ and all internal layers are simultaneously contributing to the uptake.

Computer simulations of the model described above showing the uptake of SO_2 on α-Al_2O_3 and MgO particles are presented in Figure 7 and are compared to the experimental curves determined for each mass. The experimental and fitting parameters used in the model are given in Table 2. To fully model the mass spectral curves shown in Figure 7, the initial conditions are taken as $dI/dt = I_o = 1$, during the time the sample is exposed to the surface dI/dt is given by eq 21 and when the sample lid is closed the signal increases back to its initial value according to the equation $dI/dt = k_{esc}(I_o - I)$. The model fits the general shape of the experimental data fairly well. For MgO, there is an overall better fit to the data. The model shows that

TABLE 2: Parameters Used in the Layer-by-Layer Uptake Model

	α-Al_2O_3	MgO
experimental parameters		
A_s (cm^2)	5.07	5.07
A_h (cm^2)	0.0129	0.0129
k_{esc} (s^{-1})	0.080	0.080
S_{BET} ($cm^2\ mg^{-1}$)	140	150
P (mTorr)	0.004	0.004
density, ρ (g/cm^3)	0.60	0.50
other input parameters		
N_{max} (molecules cm^{-2})	2.1×10^{13}	4.7×10^{13}
fitting parameters		
D ($cm^2\ s^{-1}$)	4.0×10^{-8}	1.6×10^{-8}
γ_o	1.0×10^{-4}	2.7×10^{-4}

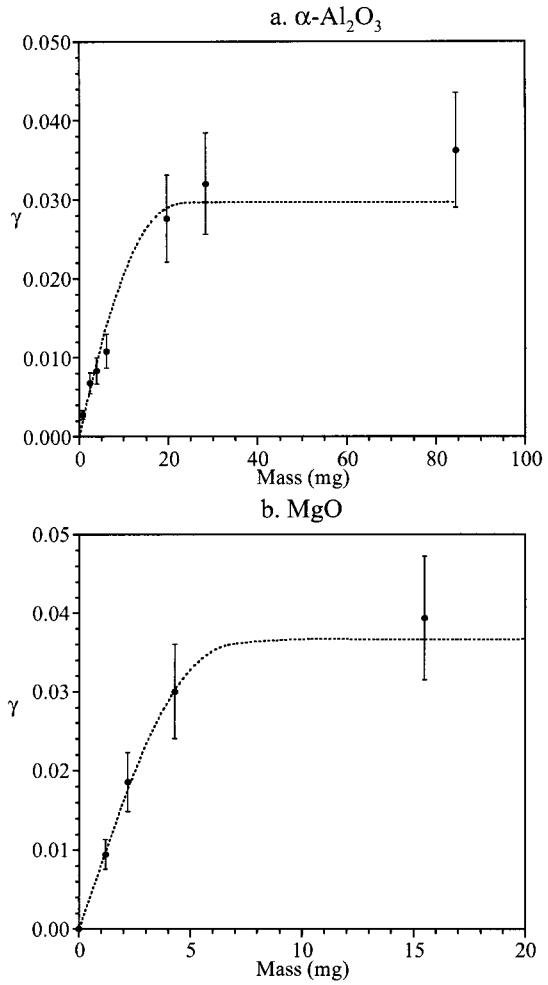

Figure 8. Experimental initial uptake coefficient plotted as a function of sample mass for (a) α-Al_2O and (b) MgO. Error bars for each of the experimental data points are estimated to be on the order of 20%. The line through the data represents the simulated uptake coefficient, using a layer by layer uptake model, as a function of sample mass. See text for further details.

the uptake decreases faster for the thinner samples and that the maximum in γ_{obs} corresponding to a minimum in the normalized QMS intensity, shifts to longer times.

There are many reasons why the model may not fit the experimental data exactly, especially at longer times. For example, the use of a Langmuir-type model to describe the surface saturation may be an oversimplifications. In addition, the use of a constant effective diffusion constant may also be an oversimplification.

The maximum in the observed uptake coefficient as a function of sample mass is plotted in Figure 8. Some additional experiments were done for SO_2 uptake on α-Al_2O_3 samples of larger mass and are included in Figure 8. The line through the data is the maximum in the uptake coefficient calculated from the model. It can be seen that there is very good agreement between the model and the experimental data. The observed uptake coefficient is linearly proportional to the mass for small sample masses. The observed initial uptake coefficient then levels off at the higher masses.

Determination of Saturation Coverages and Characterization of Gas-Phase Products from Knudsen Cell Experiments. Surface coverage can be determined using the Knudsen cell reactor by allowing the powder to completely react with the SO_2 until the SO_2 signal goes back to its baseline value and

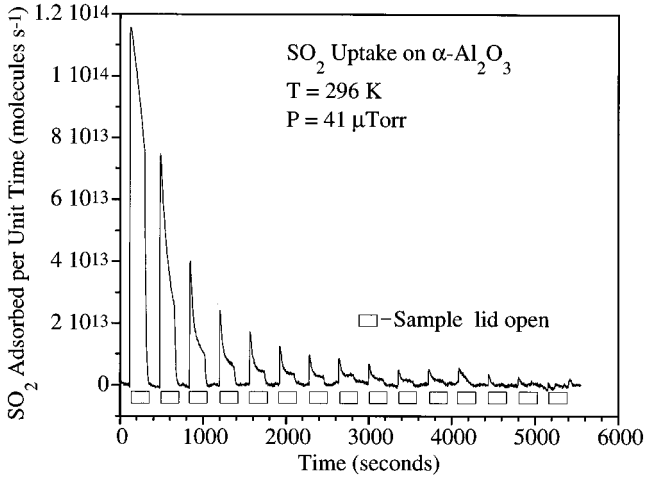

Figure 9. Total uptake of SO_2 on α-Al_2O_3 determined from calibrated Knudsen flow data. The amount of SO_2 adsorbed on the α-Al_2O_3 decreased as a function of time as the surface reached its maximum uptake. The decrease in the uptake of SO_2 molecules as a function of time follows a nearly exponential decay.

there is no longer any additional uptake. The SO_2 QMS intensity can be converted to the number of molecules lost to the surface per second as a function of time. The area under the resultant flow curve can be integrated. Conversion of QMS intensity to molecular flow was accomplished by multiplying the effective area of the escape aperture by the collision rate which yields the number of molecules per second escaping the cell as a function of pressure (molecules s^{-1} $mTorr^{-1}$). When this value is multiplied by the experimentally determined absolute pressure versus QMS intensity data (mTorr amp^{-1}), a conversion factor is obtained which could be used to convert the SO_2 QMS signal to molecular flow. This procedure was followed in order to determine surface coverages in the μTorr pressure regime. From the mass of the sample and the BET surface area, the total number of SO_2 molecules that adsorb on the surface per unit area can be determined. Surface coverages were determined at pressures above 4 μTorr in order to ensure complete saturation of the surface in a reasonable period of time. Experiments for α-Al_2O_3 and MgO were done at pressures of 41 and 202 μTorr, respectively.

The experimental data for α-Al_2O_3 are shown in Figure 9. The data shown in Figure 9 are plotted as the number of molecules of SO_2 adsorbed per second as a function of time. The flow data have been baselined to zero and inverted so that the amount of SO_2 adsorbed could be directly determined from the integration of the area under the curve shown in Figure 9. A sample mass of 2.6 mg was used in the experiment shown in Figure 9. The number of molecules adsorbed on the surface was determined from integration to be 3.8×10^{16} molecules. The surface coverage at the end of the experiment is determined to be 6.5×10^{13} molecules cm^{-2}. The decay in the flow of adsorbed SO_2 is nearly exponential. Therefore, an exponential decay was applied to the data for the smallest masses shown in Figure 6 in order to determine the maximum number of sites, N_s, that will be occupied at 4 μTorr. This number was used in the model shown in Figures 7 and 8. The values obtained for N_s at different pressures using the Knudsen cell technique as well as the values obtained for the saturation coverage in the mTorr regime determined by FTIR/volumetric measurements are given in Table 3. The maximum surface coverage must be determined at the pressure used in the uptake experiment. As shown in Table 3, the maximum surface coverage determined in the mTorr regime overestimates N_s in the μTorr regime.

TABLE 3: Number of Occupied Surface Sites, N_s, Determined from Volumetric/FT-IR and Knudsen Cell Measurements for SO_2 Uptake on α-Al_2O_3 and MgO Particles[a]

	N_s (molecules cm^{-2})		
oxide	volumetric/FT-IR data (350 mTorr)	K nudsen cell data (pressure in mTorr)	extrapolated Knudsen cell data (0.004 mTorr)
α-Al_2O_3	$1.5 (\pm 0.3) \times 10^{14}$	$6.3 (\pm 1.2) \times 10^{13}$ (0.041 mTorr)	$2.1 (\pm 0.4) \times 10^{13}$
MgO	$3.5 (\pm 0.6) \times 10^{14}$	$1.8 (\pm 0.4) \times 10^{14}$ (0.202 mTorr)	$4.7 (\pm 0.5) \times 10^{13}$

[a] Error in these measurements is estimated to be approximately 20−25% based on multiple measurements.

In addition to surface coverage and gas uptake, potential product species were monitored during these experiment, including CO_2 (*m*/*e* 44), SO_3 (*m*/*e* 80) and H_2SO_4 (*m*/*e* 98). Only CO_2 showed an increase in signal, after a short induction period, during the course of the experiments and only for MgO. This result is explained in the next section.

Discussion

Heterogeneous Uptake Kinetics Determined from Knudsen Cell Measurements. The Knudsen cell data show that gas diffusion into underlying layers occurs readily. The observed uptake coefficient calculated via eq 5 must then be corrected to take into account the additional surface area of the underlying layers. This can be done by using the BET area of the entire powder sample. This has been done for the four samples of different masses measured for α-Al_2O_3 and MgO. The values of γ are given in Table 1 where both the maximum in the observed uptake coefficient is given along with the BET corrected value for each mass. It is seen that the values of $\gamma_{max,obs}$ and $\gamma_{max,BET}$ differ by at least an order of magnitude. The value of the initial uptake used in the model is also given in Table 1. It can be seen that the value of the initial uptake coefficient used in the model is close to the value of the uptake coefficient corrected for BET area determined using masses in the linear regime for both α-Al_2O_3 and MgO as the larger masses for both α-Al_2O_3 and MgO underestimate the initial uptake coefficient. This can be understood from the data plotted in Figure 8 which shows that the higher sample masses are close to the plateau region, and therefore, the observed uptake coefficient will not scale linearly with mass and the use of the entire BET area of the sample over estimates the available surface area measured in the time it takes for the uptake coefficient to reach its maximum value. It is important to note that it is clear that the observed uptake coefficient which uses the geometric area of the sample overestimates the uptake coefficient by at least an order of magnitude.

The fact that there is such good agreement between the initial uptake coefficient determined from the model and the maximum uptake coefficient corrected for the BET area for smaller masses indicates that the surface saturation effects are not significant on the time scale of the measured γ_{max}. If the saturation effects were larger, i.e., if the *a* term defined in eq 11 was larger either because there were fewer available surface sites, the experiment was done at higher pressures or if γ_o was larger, i.e., greater than 10^{-3}, then the uptake coefficient determined using the BET area, even for small masses, would underestimate the initial uptake coefficient.

Mechanisms for SO_2 Adsorption on α-Al_2O_3 and MgO. Information about the adsorption mechanism for SO_2 on the surface may be inferred from the infrared data. Several prior studies have investigated the surface sites responsible for weakly and strongly adsorbed SO_2 following reaction of SO_2 on both alumina and magnesium oxide particles. Karge and Dalla Lana[58] studied the interaction of SO_2 with γ-alumina using infrared spectroscopy. Using site blocking experiments with ammonia, pyridine and boron trifluoride, they determined that interaction of SO_2 with basic sites on the surface leads to formation of chemisorbed SO_2 while adsorption at acid sites leads to physisorbed SO_2.

As described here, SO_2 reacts with α-Al_2O_3 particles to a small fraction of weakly adsorbed SO_2 and a larger fraction of strongly adsorbed surface-coordinated sulfite and/or bisulfite. Upon adsorption of water vapor onto sulfite coated α-Al_2O_3 particles, no new products are detected. Thus a mechanism can be postulated for SO_2 reaction on α-Al_2O_3 particles: weakly adsorbed SO_2 forms on acidic aluminum sites and surface-coordinated sulfite forms when SO_2 interacts with basic oxide anions or hydroxides on the α-Al_2O_3 surface. Datta et al.[79] further elaborated on adsorption of SO_2 on acid and base sites and proposed a mechanism for SO_2 adsorption on γ-Al_2O_3. They reported that adsorption on SO_2 on Lewis acid sites (coordinately unsaturated aluminum atoms) resulted in weakly adsorbed SO_2. Adsorption of SO_2 on Lewis base sites (exposed oxygen atoms) followed by rearrangement where the sulfite species attaches to an aluminum through the sulfur atom resulted in chemisorbed sulfite.

The surfaces investigated here are covered with hydroxyl groups at a surface coverage around 4×10^{14} molecules cm^{-2}.[80] It is possible and most likely probable that they are involved in both the weak and strongly bonded interactions with SO_2. Several different reactions can be proposed for the hydroxylated α-Al_2O_3 particle surface to yield surface coordinated sulfite and bisulfite according to reactions 25, 26, and 27 below,

$$O^{2-}(l) + SO_2 \rightarrow SO_3^{2-}(a) \quad (25)$$

$$OH^-(a) + SO_2 \rightarrow HSO_3^-(a) \quad (26)$$

$$2OH^-(a) + SO_2 \rightarrow SO_3^{2-}(a) + H_2O \quad (27)$$

where O^{2-} and OH^- are lattice oxygen atoms and adsorbed hydroxyl, respectively.

Due to the breadth of the absorption band shown in Figure 2 for SO_2 adsorption on α-Al_2O_3, it would be difficult to distinguish between these possibilities based on infrared spectroscopy alone. The OH stretching region shown in Figure 2 could be interpreted as being due the formation of strongly adsorbed water or to the OH stretch in adsorbed bisulfite. This OH bond can then hydrogen bond to nearby surface hydroxyl groups.

The surface reaction of SO_2 with MgO appears to follow a somewhat different mechanism as the MgO surface is not as hydroxylated as the α-Al_2O_3 surface investigated here. The spectroscopic data show that SO_2 reacts with MgO particles to form weakly adsorbed SO_2, surface-coordinated sulfite and bidentate sulfate. A probable mechanism for formation of weakly adsorbed SO_2 and surface-coordinated sulfite would then be similar to that postulated for α-Al_2O_3 particles: weakly adsorbed SO_2 forms on acidic magnesium sites and surface-coordinated sulfite forms when SO_2 interacts with basic oxide

anions on the MgO surface according to reaction 28.

$$MgO + SO_2 \rightarrow MgSO_3 \quad (28)$$

Pacchioni et al. conducted a theoretical study of the adsorption and reaction of SO_2 on a clean, completely dehydroxylated MgO(100) surfaces.[81] They found a similar distinction between acidic and basic sites. When SO_2 interacts with acidic Mg^{2+} sites, the bonding is largely electrostatic resulting in weakly adsorbed SO_2. When SO_2 interacts with basic O^{2-} sites strong adsorption occurs with the formation of surface sulfite. It was also determined that only O^{2-} with low coordination number, i.e., O^{2-} present at steps and kinks could react with SO_2 to form surface sulfite. Surface oxygen anions on terrace planes were found to be much less reactive toward SO_2.

In addition, because of its basic nature MgO reacts with atmospheric CO_2 to give $MgCO_3$. There is evidence in the Knudsen cell experiment that CO_2 evolves as SO_2 reacts according to reaction 29

$$MgCO_3 + SO_2 \rightarrow MgSO_3 + CO_2 \quad (29)$$

The conversion of chemisorbed sulfite to sulfate has been reported in the literature for high-temperature reactions between SO_2 and oxide surfaces in the presence of oxygen. Chang observed oxidation of adsorbed sulfite/SO_2 on γ-Al_2O_3 particles in oxygen between 400 and 500 °C to produce $Al_2(SO_4)_3$, an aluminum-sulfate-like species.[59] Martin et al. reports that $CaSO_3$ reacts with SO_2 to produce $CaSO_4$ at 200 °C, but $CaSO_4$ is not the dominate product until 750 °C is reached.[60] At room temperature, there is evidence for sulfate formation on MgO but not on α-Al_2O_3. It has been suggested in the theoretical study of Pacchioni et al. that sulfate can form by interaction of the sulfur atom in SO_2 with two surface five-coordinated O^{2-} anions, in other words two oxide anions on the unreconstructed MgO (100) surface.[81] It was predicted that the MgO(100) surface would be especially suited for $MgSO_4$ formation because the separation between the two lattice oxygens of MgO is 0.297 nm which is near the spacing of oxygens in bulk SO_4^{2-} powders, 0.270 nm. However, this structure was found to be highly repulsive and SO_2 dissociates spontaneously because the five-coordinated oxide anions do not offer enough basic character. However, four-coordinated oxide anions, which are commonly found on steps and corners of MgO (100), have more basic character. These anions may provide favorable sites for sulfate formation. The MgO particles used in this study are powders, not single crystals. Thus, the MgO particles would be expected to have more defects, steps and kinks (more four-coordinated oxide anions) available for reaction and may stabilize the formation of bidentate sulfate on MgO particles at room temperature. This may be the reason that we observe a small amount forming upon adsorption of SO_2. The conversion of sulfite to sulfate upon adsorption of water that is observed here is not well understood at this time. This reaction may be similar to gas-phase reaction 2 in that gas phase water is reacting with surface sulfite to produce surface sulfate alternatively surface adsorbed water may cause a reconstruction of the surface atoms such that additional sulfate formation is possible.

Atmospheric Implications and Conclusions. In this study, the heterogeneous uptake of SO_2 at 296 K on α-Al_2O_3 and MgO was investigated. The infrared data showed that sulfite and bisulfite formed on the surfaces at room temperature. The uptake was quantified by Knudsen cell measurements and the initial uptake coefficient was found to be in the range of 10^{-4} when surface the entire BET area was taken into account. It has been previously determined that uptake coefficients of 10^{-4} are sufficiently large such that SO_2 uptake on mineral dust could have a significant impact on the partitioning of SO_2 from the gas phase to the aerosol.[1]

Acknowledgment. The authors gratefully acknowledge the National Science Foundation (CHE-9988434) and the Department of Energy-Atmospheric Chemistry Program (DOE DE-FG02-98ER 62580) for support of this work.

References and Notes

(1) Dentener, F. J.; Carmichael, G. R.; Zhang, Y.; Leieveld, J.; Crutzen, P. J. *J. Geophys. Res*. **1996**, *101*, 22869.

(2) Song, C. H.; Phadnis, M.; Carmichael, G. R.; Underwood, G. M.; Miller, T. M.; Balster, E. T.; Grassian, V. H. *Air Pollution VII*, "*Modeling Heterogeneous Reactions in Air Pollution Models*"; WIT Press: South Hampton, Boston, 1999; pp 685−695.

(3) Parungo, F.; Kim, Y.; Zhu, C. J.; Harris, J.; Schnell, R.; Li, X. S.; Yang, D. Z.; Zhou, M. Y.; Chen, Z.; Park, K.; STC Rep. 2906; Natl. Oceanic and Atmos. Admin. Air Resource Lab: Silver Spring, MD, 1995.

(4) Silva, P. J.; Carlin, R. A.; Prather K. A. *Atmos. Environ.* **2000**, *34*, 1811−1820.

(5) Savoie, D. L.; Prospero, J. M.; Saltzman, E. S., *J. Geophys. Res.* **1989**, *94*, 5068−5080.

(6) Savoie, D. L.; Prospero, J. M.; Arimoto, R.; Duce, R. A. *J. Geophys. Res.* **1994**, *99*, 3587−3596.

(7) Li-Jones, X.; Prospero, J. M. *J. Geophys. Res.* **1998**, *103*, 16073−16084.

(8) Talbot, R. W.; Harris, R. C.; Browell, E. V.; Gregory, G. L.; Sebacher, D. I.; Beck, S. M. *J. Geophys. Res.* **1986**, *91*, 5173−5182.

(9) Cunningham P. T.; Johnson, S. A.; Yang, R. T. *Environ. Sci. Technol.* **1974**, *8*, 131−135.

(10) Levin, Z.; Ganor, C.; Gladstein, V. *J. Appl. Meteor*. **1996**, *35*, 1511−1523.

(11) Hobert, H. *Vib. Spectrosc*. **1995**, *9*, 169−179.

(12) Wall, S. M.; John, W.; Ondo, J. L. *Atmos. Environ.* **1988**, *22*, 1649−1656.

(13) Wolff, G. T. *Atmos. Environ.* **1987**, *17*, 1733−1738.

(14) Dlugi, R.; Jordan, S.; Lindemann, E. *J. Aerosol Sci.* **1982**, *13*, 190−191.

(15) Mamane Y.; Gottlieb, J. *J. Aerosol Sci*. **1990**, *21*, S225−S228.

(16) Judiekis, H. S.; Stewart, T. B.; Wren, A. G. *Atmos. Environ.* **1978**, *12*, 1633−1641.

(17) Dlugi, R.; Jordan, S.; Lindeman, E. *J. Aerosol Sci.* **1981**, *12*, 185−197.

(18) Underwood, G. M.; Miller, T. M.; Grassian, V. H. *J. Phys. Chem. A* **1999**, *103*, 6184−6190.

(19) Goodman, A. L.; Underwood, G. M.; Grassian, V. H. *J. Phys. Chem. A* **1999**, *103*, 7217−7223.

(20) Underwood, G. M.; Li, P.; Usher, C. R.; Grassian V. H. *J. Phys. Chem. A* **2000**, *104*, 819−829.

(21) Goodman, A. L.; Underwood, G. M.; Grassian V. H. *J. Geophys. Res.- Atmos.* **2000**, *104*, 29053.

(22) Underwood, G. M.; Song, C. H.; Phadnis, M.; Carmichael; G. C.; Grassian V. H. *J. Geophys. Res.-Atmos.* **2001** (in press).

(23) Borensen, C.; Kirchner, U.; Schear, V.; Vogt R.; Zellner, R. *J. Phys. Chem. A* **2000**, *104*, 5036−5045.

(24) Fenter, F. F.; Caloz, F.; Rossi, M. J. *Atmos. Environ.* **1995**, *29*, 3365−3372.

(25) Finlayson-Pitts, B. J.; Pitts, J. N. *Atmospheric Chemistry: Fundamental and Experimental Techniques*; Wiley: New York, 1986.

(26) Sievering, H.; Boatman, J.; Gorman, E.; Kim, Y.; Anderson, L.; Ennis, G.; Luria, M.; Pandis, S. *Nature* **1992**, *360*, 571−573.

(27) Sievering, H.; Boatman, J.; Galloway, J.; Keene, W.; Kim, Y.; Luria, M.; Ray, J. *Atmos. Environ.* **1991**, *25A*, 1479−1487.

(28) Sievering, H.; Gorman, E.; Pszenny, A.; Springer-Young, M.; Boatman, J.; Kim, Y.; Nagamoto, C.; Wellman, D *J. Geophys. Res.* **1995**, *100*, 23075−23081.

(29) Chameides, W. L.; Stelson, A. W. *J. Geophys. Res.* **1992**, *97*, 20565−20580.

(30) Suhre, K.; Andrea, M. O.; Rosset, R. *J. Geophys. Res*. **1995**, *100*, 11323.

(31) Keene, W. C.; Sander, R.; Pszenny, A. A. P. *J. Aerosol Sci.* **1998**, *29*, 339.

(32) Luria, M.; Sievering, H. *Atmos. Environ*. **1991**, *25A*, 1489.

(33) Capaldo, K.; Corbett, J. J.; Kasibhatla, P.; Fischbeck, P.; Pandis, S. N. *Nature* **1999**, *400*, 743−746.

(34) Krischke, U.; Staubes, R.; Brauers, T.; Gautrois, M.; Burkert, J.; Stobener, D.; Jaeschke, W. *J. Geophys. Res*. **2000**, *105*, 14413−14422.

(35) Jayne, J. T.; Duan, S. X.; Davidovits, P.; Worsnop, D. R.; Zahniser, M. S.; Kolb, C. E. *J. Phys. Chem.* **1992**, *96*, 5452−5460.
(36) Martin, L. R.; Good, T. W. *Atmos. Enrviron*. **1991**, *25A*, 2395−2399.
(37) Worsnop, D. R.; Zahniser, M. S.; Kolb, C. E.; Gardner, J. A.; Watson, L. R.; Van Doren, J. M.; Jayne, J. T.; Davidovits, P. *J. Phys. Chem.* **1989**, *93*, 1159−1172.
(38) Liang, J.; Jacobson, M. Z. *J. Geophys. Res.* **1999**, *104*, 13749−13769.
(39) Davidovits, P.; Jayne, J. T.; Worsnop, D. R.; Zahniser, M. S.; Kolb, C. E. *J. Phys. Chem.* **1990**, *94*, 6041−6048.
(40) Saxena, P.; Seigneur, C. *Atmos. Environ.* **1987**, *21*, 807−812.
(41) Boniface, J.; Shi, Q.; Li, Y. Q.; Cheung, J. L.; Rattigan, O. V.; Davidovits, P.; Worsnop, D. R.; Jayne, J. T.; Kolb, C. E. *J. Phys. Chem. A* **2000**, *104*, 7502−7510.
(42) Dlugi, R. *J. Aerosol Sci.* **1983**, *14*, 292−7.
(43) Maahs, H. G. *J. Geophys. Res.* **1983**, *88*, 721.
(44) Kerminen, V.; Pirjola, L.; Boy, M.; Eskola, A.; Teinila, K.; Laakso, L.; Asmi, A.; Hienola, J.; Lauri, A.; Vainio, V.; Lehtinen, K.; Kulmala, M. *Atmos. Res.* **2000**, *54*, 41−57.
(45) Hegg, D. A.; Majeed, R.; Yuen, P. F.; Baker, M. B.; Larson, T. V. *Geophys. Res. Lett.* **1996**, *23*, 2613−2616.
(46) Han, J. H.; Martin, S. T. *J. Geophys. Res.-Atmos.* **1999**, *104*, 3543−3553.
(47) Martin, S. T. *Chem. Rev.* **2000**, *100*, 3403−3453.
(48) Golden, D. M.; Spokes, G. N.; Benson, S. W. *Angew. Chem.* **1973**, *12*, 534−546.
(49) Dushman, S. *Scientific Foundations of Vacuum Technique*, 2nd ed.; Wiley: New York, 1962.
(50) Underwood, G. M.; Li, P.; Usher, C. R.; Grassian V. H. *J. Phys. Chem. A* **2000**, *104*, 819.
(51) Waqif, M.; Saad, A. M.; Bensitel, M.; Bachelier, J.; Saur, O.; Lavalley, J. *J. Chem. Soc., Faraday Trans.* **1992**, *88*, 2931−2936.
(52) Lin, M. J.; Lunsford, J. H. *J. Phys. Chem.* **1975**, *79*, 892−897.
(53) Ziolek, M.; Kujawa, J.; Saur, O.; Aboulayt, A.; Lavalley, J. C. *J. Mol. Catal. A: Chem.* **1996**, *112*, 125−132.
(54) Lavalley, J. C.; Janin, A.; Preudhomme, J. *React. Kinet., Catal. Lett.* **1981**, *18*, 85−88.
(55) Nakamoto, K. *Infrared Spectra of Inorganic and Coordination Compounds*, 4th ed.; John Wiley and Sons: New York, 1986.
(56) Herzberg, G. *Molecular Spectra and Molecular Structure*, Vol. 1; Van Nostrand: Princeton, 1950.
(57) Mitchell, M. B.; Sheinker, V. N.; White, M. G. *J. Phys. Chem.* **1996**, *100*, 7550−7557.
(58) Karge, H. G.; Dalla Lana, I. G. *J. Phys. Chem.* **1984**, *88*, 1538−1543.
(59) Chang, C. C. *J. Catal.* **1978**, *53*, 374−385.
(60) Martin, M. A.; Childers, J. W.; Palmer, R. A. *Appl. Spectrosc.* **1987**, *41*, 120−126.
(61) Babaeva, M. A.; Tsyganenko, A. A.; Filimonov, V. N. *Kinet. Catal.* **1984**, *25*, 787.
(62) Schoonheydt, R. A.; Lunsford, J. H. *J. Catal.* **1972**, *26*, 261−271.
(63) Gebel, M. E.; Finlayson-Pitts, B. J. *Geophys. Res. Lett.* **2000**, *27*, 887−890.
(64) Calvert, J. G.; Pitts, J. N. *Photochemsitry*, Wiley: New York, 1966.
(65) Goodman, A. L. Ph.D. Dissertation, The University of Iowa, 2000.
(66) Stark, J. V.; Park, D. G.; Lagadic, I.; Klabunde, K. *J. Chem. Mater.* **1996**, *8*, 1904−1912.
(67) Beichert, P.; Finlayson-Pitts, B. J. *J. Phys. Chem.* **1996**, *100*, 15218.
(68) Davies, J. A.; Cox, R. A. *J. Phys. Chem.* **1998**, *102*, 7631.
(69) Vogt R.; Finlayson-Pitts, B. J. *J. Phys. Chem.* **1994**, *98*, 3747.
(70) Ghosal, S.; Hemminger, J. C. *J. Phys. Chem. A* **1999**, *103*, 4777.
(71) Goodman, A. L.; Bernard, E. T.; Grassian, V. H. *J. Phys. Chem. A* **2001**, in press.
(72) Miller, T. M.; Grassian, V. H. *Geophys. Res. Lett.* **1998**, *25*, 3835.
(73) Nakamoto, K.; Fujita, J.; Tanaka, S.; Kobayashi, M. *J. Am. Chem. Soc.* **1957,** *79*, 4904.
(74) Bhagavantam, S.; Venkatarayudu, T. *Indian Acad. Sci.* **1939**, *9A*, 224−258.
(75) Golden, D. M.; Manion, J. A. *Advances in Chemical Kinetics and Dynamics* Vol. 1; JAI Press: 1992, 187−276.
(76) Li, P.; Grassian, V. H. *J. Phys. Chem.*. submitted.
(77) Atkins, P. *Physical Chemistry*, 6th ed.; W. H. Freeman and Company: New York, 1998, p 754.
(78) Crank, J. *Mathematics and Diffusion*, 2nd ed; Oxford Science Publications; 1975; p 21.
(79) Datta, A.; Cavell, R. G.; Tower, R. W.; George, Z. M. *J. Phys. Chem.* **1985**, *89*, 443.
(80) Knozinger, H.; Ratnasamy, P. *Catal. Rev. Sci. Eng.* **1978**, *17*, 31.
(81) Pacchioni, G.; Clotet, A.; Ricart, J. M. *Surf.ace Sci.ence* **1994**, *315*, 337−350.